Local DEM Compensation for Along-Track SAR Formations

Naomi Petrushevsky
Department of Electronics, Information and Bioengineering
Politecnico di Milano
Milan, Italy
naomi.petrushevsky@polimi.it

Andrea Monti Guarnieri
Department of Electronics, Information and Bioengineering
Politecnico di Milano
Milan, Italy
andrea.montiguarnieri@polimi.it

Marco Manzoni
Department of Electronics, Information and Bioengineering
Politecnico di Milano
Milan, Italy
marco.manzoni@polimi.it

Abstract—Along-track formations of small satellites are of great interest for future Synthetic Aperture Radar (SAR) systems since they can image at high resolution over wide swaths. Each sensor operates with reduced pulse-repetition-frequency (PRF), which causes significant azimuth ambiguities. However, these ambiguities can be removed by a well-known multichannel recombination that is effective only if the cross-track (XT) baseline between sensors is kept negligible. This work proposes a post-processing approach to mitigate the residual ambiguities caused by small XT baselines based on the knowledge of the scene's Digital Elevation Model (DEM). The method has been validated with simulated data, considering a realistic distributed scene.

Index Terms—SAR, SIMO, image formation, azimuth ambiguities, DEM.

I. Introduction

Synthetic Aperture Radar (SAR) is a mature remote sensing technology that provides repeated observations regardless of illumination conditions and weather disturbances. Future improvement in performance, in terms of resolution and swath size, can be achieved by distributing the sensing load on different spacecraft [1]. Small satellites, e.g., Cubesats, are particularly interesting since they can provide a low-cost and robust alternative to the single-sensor paradigm [2].

According to the Along-Track (AT) SAR formation concept [3], one can reconstruct an equivalent monostatic acquisition from a set of under-sampled bistatic acquisitions, given that all receivers travel in a tight formation. The sensors follow the same orbit but are shifted in their relative AT positions. Each satellite under-samples the scene, causing severe azimuth ambiguities that are resolved by coherently combining the different channels. In a standard SAR system, fine azimuth resolution demands a high Pulse Repetition Frequency (PRF) that, in turn, limits the maximum swath depth. This limitation is relaxed by properly placing multiple sensors along-track, each operating with a reduced PRF, then keeping the swath large.
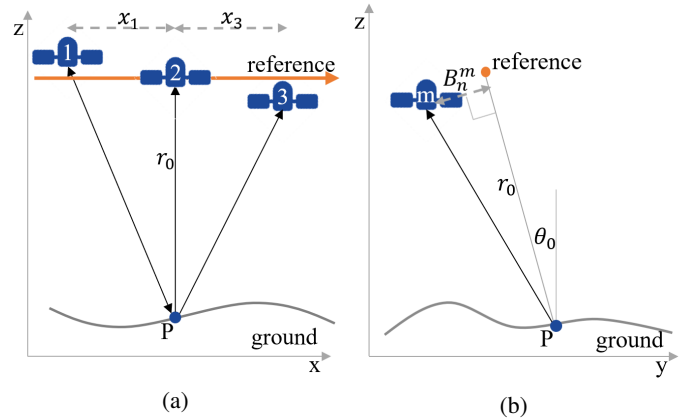

Fig. 1: System geometry for a formation of three satellites. (a) X-Z projection, the satellites are displaced along the AT direction. (b) Y-Z projection, each satellite is defined also by a displacement perpendicular to the AT axis. For simplicity, the second satellite is assumed to be the reference.

The successful generation of a SAR image from different under-sampled bistatic acquisitions is possible if the orbits are kept under tight control. However, realistic spacecraft experience orbital errors in the AT and cross-track (XT) directions. The geometry of the multi-channel system is shown in Fig.1. The limits and solutions for the AT deviations are well covered in literature [1], [4], [5]. XT baselines interfere with combining different SAR channels, as phase disturbances are introduced, proportional to the aforementioned baselines and the observed topography [3], [6]. If the elevation is almost flat or does not significantly vary in the azimuth direction, it is possible to compensate for the phase excursions as described in [7], [8]. However, local elevation changes introduce additional complexity that must be solved.

In this work, we first demonstrate how topography interferes with the standard method for channel combination. Then, we propose a processing scheme to mitigate the ambiguities

due to uncompensated phase contributions by accounting for local elevation changes. The compensation is performed in the focused data domain to cope with space-variant phase errors. It is implemented as a post-processor that operates on images focused and co-registered by standard tools. Finally, validation is presented with simulated data, considering a realistic radar cross-section (RCS) map obtained from a stack of COSMO-SkyMed acquisitions.

II. PROBLEM STATEMENT

A. Ideal formation

Let us first consider an ideal case where M satellites follow the ideal orbit with no XT baselines, and each receiver undersamples in azimuth by a factor N_r, with respect to the antenna SAR Doppler bandwidth, $2v_s/L_a$, L_a being the antenna length. This causes the data acquired from a single channel to be aliased:

$$U_{m,0}(k_x, k_r') = \sum_i Z_0 \left(k_x + ik_{xs}, k_r'\right) \\ \cdot \exp\left(jk_x \frac{x_m + x_{tx}}{2}\right) \exp\left(j\Phi_{m,i}^{AT}\right) \tag{1}$$

$$\Phi_{m,i}^{AT} = ik_{xs} \frac{x_m + x_{tx}}{2} - \frac{\Omega_0}{4r_0}(x_m - x_{tx})^2, \tag{2}$$

k_x being the azimuth wavenumber, $k_r' = k_r - \Omega_0$ the base-band range wavenumber, $\Omega_0 = 4\pi/\lambda$, where λ is the wavelength. x_m and x_{tx} are the AT displacements of receiver m and the transmitter tx from the reference orbit, r_0 is the zero-Doppler distance, and $k_{xs} = 2\pi/dx$, dx being the Azimuth sampling interval. Finally, Z_0 is the spectrum of the equivalent monostatic Range Compressed (RGC) data:

$$Z_0(k_x, k_r') = D_0(k_x, k_r')G_a(k_x)H_s(k_x, k_r') \tag{3}$$

where D_0 is the spectrum of the scene, G_a is the antenna pattern, and H_s accounts for the SAR acquisition:

$$G_a(k_x) \approx \text{sinc}^2\left(\frac{L_a}{4\pi}k_x\right) \tag{4}$$

$$H_s(k_r, k_x) \approx \exp\left(j\frac{r_0}{2\Omega_0}\left(k_x^2 - \frac{k_x^2 k_r'}{\Omega_0}\right)\right) \tag{5}$$

We assume a rectilinear orbit and zero squint for simplicity, but the same concepts can be adjusted to more complex orbital models [9].

The first exponential in (1) accounts for the azimuth shift of the m-th channel, w.r.t the reference, while the second one is a constant phase, different for each spectral replica, i. Theoretically, the index i can take infinite values, but in practice, it is limited by the antenna pattern. For the system described in Table I, where a down-sampling factor is $N_r = 3$, the significant values of i are $[-1, 0, 1]$.

Ideal recombination of M channels is possible when all satellites follow the anti displaced-phase-center-antenna (DPCA) condition [10]:

$$x_m^{ideal} = 2dx \cdot \frac{m-1}{m} + \mu \cdot dx \tag{6}$$

where μ is an integer number, which does not affect the system's performance and allows for safe distancing between the receivers. It is assumed that μ is significantly smaller than the antenna footprint, so all receivers share the same Doppler support [11].

If the condition in (6) holds, at least up to a certain level of accuracy, it is possible to recover the unambiguous signal by solving a set of M equations with N_r unknowns [5], expressed in matrix form as:

$$U_0(k_x) = \Gamma_0(k_x) \cdot Z_0(k_x) + W(k_x) \tag{7}$$

where U_0 is an $M \times 1$ vector of observations for a single frequency bin, Γ_0 is a matrix of $M \times N_r$ elements, each described by the exponentials in (1), and Z_0 is a $M \times 1$ vector of unfolded spectral components of the desired signal. W is the spectrum of the noise. The dependency of all the components in (7) on the angular frequency k_x was omitted for brevity, but it is important to note that the system should be solved for each frequency bin separately.

B. Cross-track baseline

Let us now introduce the effect of the XT baseline. Specifically, we are interested in the component parallel to the line-of-sight (LOS) B_n, which adds an additional path that changes in range and azimuth [12]:

$$\Delta r_m(x, r) \approx \frac{B_n^m \cdot r}{r_0 \tan\left(\theta_0(x,r)\right)} + \frac{B_n^m \cdot q(x,r)}{r_0 \sin\left(\theta_0(x,r)\right)}, \tag{8}$$

where q is the local elevation registered on the azimuth and slant-range coordinates, and θ_0 is the relevant incidence angle. The approximation in (8) is valid when the bistaticity along-track is negligible w.r.t the synthetic aperture and when $B_n \ll r_0$. Moreover, minor variations in range due to the cross-track baseline during the synthetic aperture are neglected. Finally, for the sake of simplicity, we focus on the variations in elevation throughout the scene, assuming that the baseline is constant during the acquisition. However, the derivation can account for variations in B_n similarly.

The additional path in (8) consists of two parts: the flat-earth component is proportional to the slant range, while the local topography causes the second term. They both result in a shift between the images and an additional phase: $-4\pi\Delta r_m(x,r)/\lambda$.

The spectrum of the RGC signal, affected by an XT baseline, can be expressed as:

$$U_m(k_x, k_r') = \sum_i Z_m \left(k_x + ik_{xs}, k_r'\right) H_s(k_x, k_r') \\ \cdot \exp\left(jk_x \frac{x_m + x_{tx}}{2}\right) \exp\left(\Phi_{m,i}^{AT}\right) \tag{9}$$

$$Z_m(k_x, k_r') = \mathscr{F}\left[\left(d_0(x,r) \cdot \exp\left(-j\frac{4\pi}{\lambda}\Delta r_m(x,r)\right)\right) \\ * \delta(r - \Delta r_m(x,r))\right]_{k_x, k_r'} \cdot G_a(k_x) \tag{10}$$
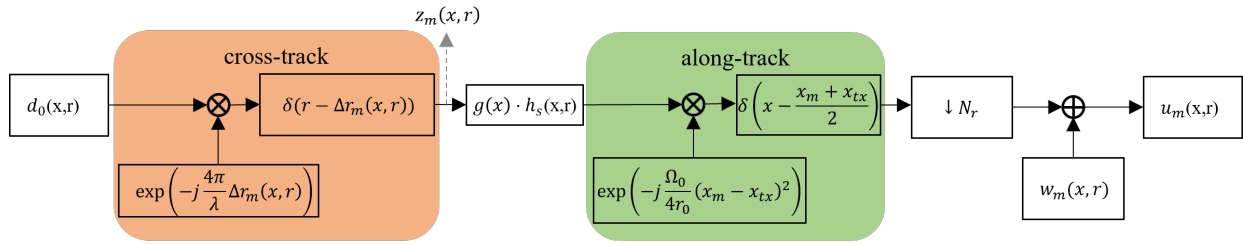
Fig. 2: Forward model of a single RGC data.

being d_0 the complex reflectivity of the scene. The model derived above is presented schematically in Fig. 2.

From (10), the equivalent monostatic acquisition differs for each satellite because of the cross-track baseline. In the frequency domain, the topographic phase imposed by (8) is convolved with the signal spectrum, preventing a proper reconstruction of the full resolution signal by (7). It is not feasible to compensate for the position-dependent effect of topography in (8) from the RGC data since each target contributes to the entire antenna aperture, which extends for kilometers.

III. CROSS-TRACK BASELINE COMPENSATION

A. Imaging

Before the compensation of the topographic phases induced by (8), we first generate M focused images. The sequence of operations we applied to each RGC data is summarized in Fig.3. The motivation for using focused images is that in the RGC domain, each target is spread over a vast span of samples, and there is no way to compensate all targets for the varying topographic effect. Thus, each channel is focused by the operator phase matched to (5), i.e., the standard $W - k$ scheme described in [9]. The combination of channels is then applied on focused images, after having properly estimated the AT and XT baselines, which is performed by standard interferometric methods.

We aim to obtain an image with an azimuth spectrum that is N_r times wider than the actual sampling. As Fig.3 shows, the first step is to up-sample the raw data (range compressed) by the same factor N_r. This is implemented, as usual, by inserting $N_r - 1$ zeros between each azimuth sample, and the effect is to replicate the azimuth spectrum N_r times. Then, data are focused by the matched phase reference. The spectra of the focused data can be expressed as follows:

$$A_m(k_x, k_r') = \sum_i Y_{m,i}(k_x, k_r')$$
$$\cdot \exp\left(jk_x \frac{x_m + x_{tx}}{2}\right) \exp\left(j\Phi_m^{AT}\right) \quad (11)$$
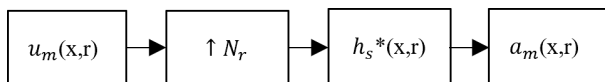

Fig. 3: Imaging processor that is applied to each RGC channel (u_m) before compensating AT and XT baselines.

$$Y_{m,i}(k_x, k_r') = Z_m(k_x + ik_{xs}, k_r')$$
$$\cdot \exp\left(j\Phi_{amb-i}(k_x, k_r')\right) \quad (12)$$
$$\cdot \exp\left(jk_x \Delta x_i\right) \exp\left(jk_r' \Delta r_i\right)$$

$$\Phi_{amb-i} = \frac{r_0(i \cdot k_{xs})^2}{2\Omega_0} - \frac{i \cdot r_0 k_r' k_x k_{xs}}{\Omega_0^2} \quad (13)$$

where Δx_i and Δr_i are the known displacements of the ambiguity in azimuth and range, respectively [13]:

$$\Delta x_i = i \frac{r_0 k_{xs}}{\Omega_0} \quad (14)$$

$$\Delta r_i = -\frac{r_0(ik_{xs})^2}{2\Omega_0^2} \quad (15)$$

Thus, the focused image consists of true targets ($i = 0$) and ambiguities ($i \neq 0$) that are defocused and shifted in azimuth and range. The additional phase of each replica (13) consists of two terms. The first term is constant, accounting for the distance between the ambiguous target and the center of the synthetic aperture. The second term accounts for the uncompensated distance variation over the synthetic aperture, which introduces a blurring of the ambiguity that spreads over multiple pixels [14].

The target and its ambiguities should be corrected for the same shift $\Delta r_m(x, r)$ (8); however, they are in different positions. Since targets and ambiguities overlap, it is not straightforward to perform the compensation. This task is described in the following section.

B. Local Ambiguity Suppression

As discussed in Section III-A, it is not feasible to compensate the position-dependent effect of topography in (8) from the RGC data since each target is spread over a large number of pixels in slow-time. After focusing, the extent of a single target is limited to several pixels. In natural scenarios, the topography slowly varies w.r.t the target's size, and we can perform the cross-track baseline compensation locally. The complete scheme of the proposed method is shown in Fig.4.

In the following analysis, we consider a local window in the focused data domain:

$$|x - x_{loc}| \leq N_x \cdot dx$$
$$|r - r_{loc}| \leq N_r \cdot dr \quad (16)$$

where dr is the slant-range sampling interval, and (x_{loc}, r_{loc}) are the coordinate of the window's center. N_x and N_r are the
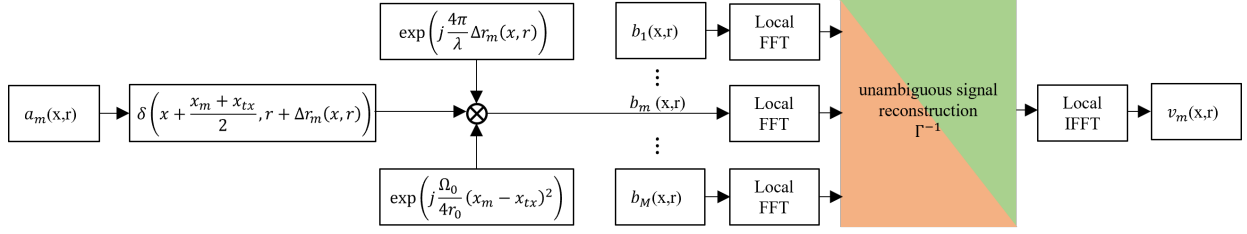
Fig. 4: Proposed processing for obtaining the unambiguous signal, where each channel is affected by a different cross-track baseline.

number of pixels in the window. For the confined window in (16), the shifts in (8) can be approximated by a linear plane:

$$\Delta r^{loc}{}_m(x_{loc}, r_{loc}) \approx$$
$$p_{m,0} + p_{m,x} \cdot (x - x^{loc}) + p_{m,r} \cdot (r - r^{loc}) \quad (17)$$

where $p_{m,0}$ is the mean displacement in the window, and $p_{m,x}, p_{m,r}$ are the linear variations in azimuth and range, respectively.

In the transformed domain, the simplified model in (17) amounts to a linear phase plane:

$$\Phi^{xt}_m(k_x, k'_r) = \frac{2\pi}{\lambda} p^0_m + k_x \cdot p^x_m + k'_r \cdot p^r_m \quad (18)$$

Theoretically, the local topography also induces a wavenumber shift [15], i.e., the span of frequencies observed by each satellite is different. However, we assume that the cross-track baseline is sufficiently small such that the wavenumber shift is negligible w.r.t the overall bandwidths.

The locally transformed signal, after upsampling and focusing as described in Section III-A, can be derived from (11) and (18):

$$A^{loc}_m(k_x, k'_r) = \sum_i Y^{loc}_{m,i}(k_x, k'_r)$$
$$\exp\left(jk_x \frac{x_m + x_{tx}}{2}\right) \exp\left(j\Phi^{AT}_m\right) \quad (19)$$

$$Y^{loc}_{m,i}(k_x, k'_r) = D^i_0(k_x + ik_{xs}, k'_r)G_a(k_x + ik_{xs})$$
$$\exp\left(j\Phi^{xt}_{m,i}\right)\exp\left(j\Phi_{amb-i}(k_x, k'_r)\right) \quad (20)$$

$$D^i_0(k_x, k'_r) = \mathcal{F}\left(d_0(x - \Delta x_i, r - \Delta r_i)\right)\big|_{k_x, k'_r} \quad (21)$$

where D^i_0 is the spectrum of the signal displaced by $(\Delta x_i, \Delta r_i)$, and $\Phi^{xt}_{m,i}$ is the phase term from (18), being (p^0_m, p^x_m, p^r_m) the relevant coefficients for the window centered around $(x^{loc} - \Delta x_i, r^{loc} - \Delta r_i)$.

After all images are focused, we proceed with coregistration, i.e., shifting each image according to the relevant AT and XT baselines, considering the known DEM. Finally, the phase screens imposed by the different baselines are removed. Both coregistration and phase compensation steps are proper for the true targets and do not consider the presence of ambiguity. At this point, the signal from (19) becomes:

$$B^{loc}_m(k_x, k'_r) = \sum_i V^{loc}_i(k_x, k'_r)$$
$$\cdot \exp\left(j\Phi^{AT}_{m,i}\right)\exp\left(j\Delta\Phi^{xt}_{m,i}(k_x, k'_r)\right) \quad (22)$$

TABLE I: Parameters of the simulated system.

Parameter	Symbol	Value
Wavelength	λ	3.12cm
Antenna length	L_s	3m
Azimuth sampling interval	dx	3m
Zero-doppler distance	r_0	570km
Number of satellites	M	3
Satellites relative positions	x_m	[-122m, 0, 122m]
Normal baselines	B^m_n	[-3m, 0, 3m]

$$V^{loc}_i(k_x, k'_r) \approx D^i_0(k_x + ik_{xs}, k'_r)$$
$$\cdot G_a(k_x + ik_{xs}) \exp\left(j\Phi_{amb-i}(k_x, k'_r)\right) \quad (23)$$

where $\Delta\Phi^{xt}_{m,i}$ is the difference between the actual topographic phase for the aliased component i and the phase that was compensated from the data:

$$\Delta\Phi^{xt}_{m,i}(k_x, k'_r) = \Phi^{xt}_{m,i}(k_x, k'_r) - \Phi^{xt}_{m,0}(k_x, k'_r) \quad (24)$$

Note that in (22), we have omitted the azimuth and range wavenumber shifts, as described above. Moreover, the spectral shifts affect the ambiguity phase Φ_{amb-i}, adding a linear phase plane for each replica in range and azimuth. However, the effect is minor and can be neglected.

The expression in (23) is not dependent on the channel index and represents the spectral components that should be reconstructed. Thus, the solution in (7) can be expanded to account for the local topography when locally processing the focused data:

$$B^{loc} = \Gamma \cdot V^{loc} + W \quad (25)$$

being Γ the $M \times N_r$ forward matrix described in (22), B^{loc} and V^{loc} are the vectors of observations and unknowns, respectively, and W is the spectrum of the noise. Similarly to (7), the system in (25) should be solved for each frequency bin separately.

Assuming that the data covariance is white and unitary and that the covariance of the noise is white with power σ^2_w, the system in can be inverted with minimum mean squared error:

$$\tilde{V}^{loc} = \Gamma^*_w \cdot B_{loc} \quad (26)$$

$$\Gamma_w = \left(\Gamma^* \cdot \Gamma + \sigma^2_w I\right)^{-1} \cdot \Gamma \quad (27)$$

V^{loc} contains N_r different elements, one for each index i. As we are interested in the spectrum of the true targets, we select only the term corresponding to $i = 0$. The other terms are
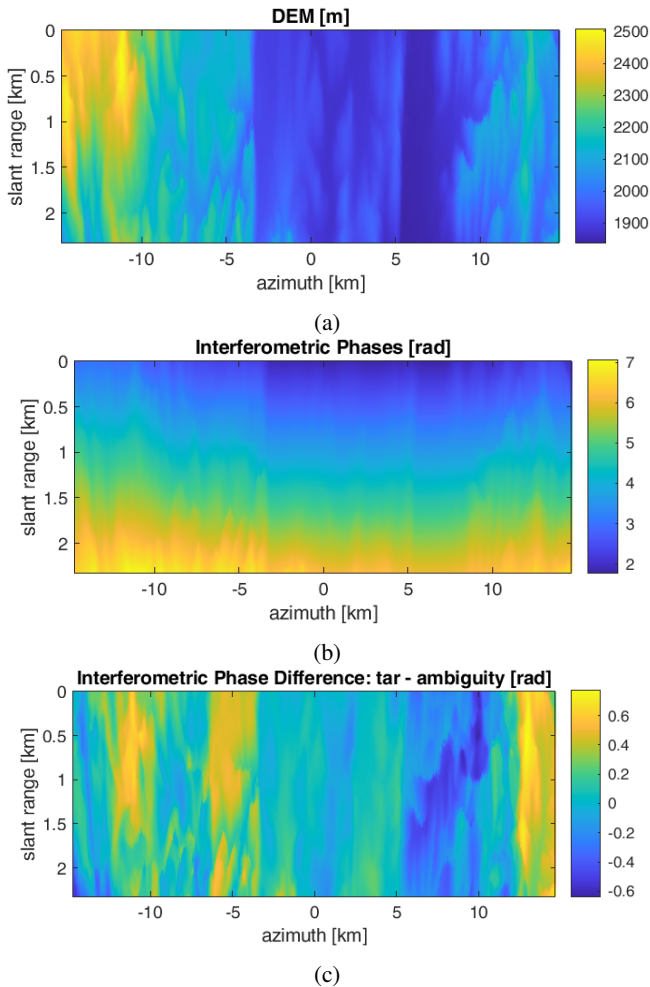
(a)

(b)

(c)

Fig. 5: Topography and its effect of the interferometric phase. (a) DEM of the scene. (b) Interferometric phase caused by the extra path in (8) for $B_n = 3m$. (c) Interferometric phase difference between the position of the target and its first ambiguity.

related to defocused ambiguities. Finally, we apply an inverse-FFT on the reconstructed spectrum to obtain the unambiguous signal in (x^{loc}, r^{loc}).

IV. RESULTS

The proposed method was validated on simulated data using the X-band system described in Table I. Regarding the orbits, ideal AT positions and non-zero XT baselines were assumed between the spacecraft. Small XT baselines were considered since the orbit control should be tight to satisfy the AT requirements [5]. However, it will be shown that even tiny deviations from the ideal orbit can deteriorate the quality of the final image.

For comparison, we consider the standard processing presented in Section II-A, which does not account for XT baselines. The only modification applied to the reference method is that the flat-earth shift from (8) and its proportional phase were compensated from the RGC data. The alteration is trivial and is justified since a single target in the RGC data occupies
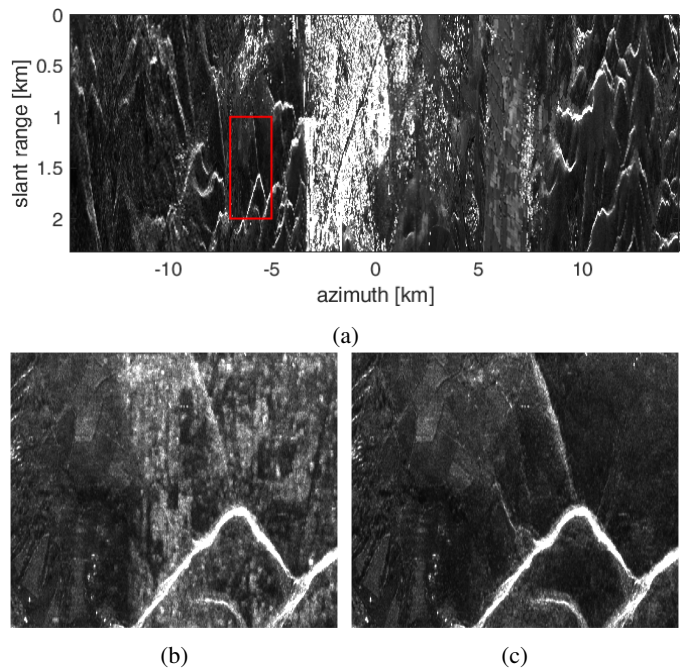

(a)

(b)

(c)

Fig. 6: Distributed scene, simulated from a realistic reflectivity map. (a) Reference reflectivity map. (b) Combination of RGC channels, according to (7). The range-dependent phase deviations between the channels were compensated before the combination. (c) Result with XT compensation. (b) and (c) refer to the region marked in red in (a).

many pixels in slow time but much less in fast time. Using the modified version of the traditional algorithm, one can better appreciate the effects of azimuth-varying topography. The latter cannot be removed from the RGC data and, as will be shown, causes significant disturbances.

A set of M RGC data was simulated, with a reflectivity map obtained by averaging a stack of COSMO-SkyMed images. The topography of the observed region is shown in Fig.5a, where it was projected to the azimuth and slant-range domain. The interferometric phases for $B_n = 3m$ are presented in Fig.5b, characterized by a strong range-dependant component and local variations imposed by the topography. Fig.5c shows the difference in interferometric phase between the targets and overlapping ambiguity $\Phi_{m,i}^{xt}(0,0)$ for $i = 1$ (see (24)). The latter can be interpreted as the phase error added to the ambiguity when compensating the interferometric phases from real targets. This error is then resolved by the inversion in (25).

The reference reflectivity map is shown in 6a. It was derived by averaging 80 COSMO-SkyMed intensity images. Following the traditional processing scheme, which reconstructs the wide-band spectrum before focusing, without accounting for XT baselines, yields the result shown in Fig.6b. Some disturbances are observed over the entire image caused by the uncompensated interferometric phases. The power of the residual ambiguities depends on the phase errors in Fig.5c and the power of the targets. Finally, using the proposed method, the intensity image in Fig.6c is a proper reconstruction of the reference data.
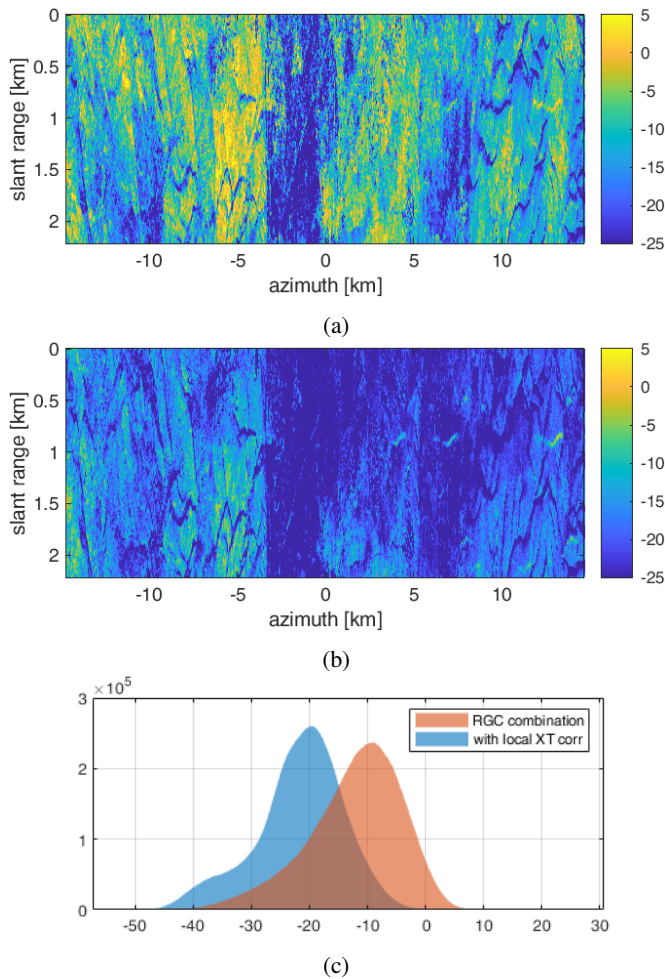
(a)

(b)

(c)

Fig. 7: AASR evaluation in dB. (a) Combination of RGC channels. (b) with the proposed method. (c) AASR Histogram, comparing the two methods.

To further appreciate the impact of ambiguities in Fig.6, we have derived an estimate of the Azimuth Ambiguity to Signal Ratio (AASR) by computing the coherence γ between the obtained results and an ideal multi-channel acquisition (no XT baselines). The relation between AASR and coherence is:

$$AASR = \gamma^{-1} - 1 \qquad (28)$$

The estimated AASR for both methods is shown in Fig.7, where there is a clear improvement after applying the local compensation. A histogram of AASR values is presented in 7c, showing a reduction of 10dB in the peak value.

V. Discussions

A novel method for compensating non-zero XT baselines for an AT SAR formation was presented in this work. The approach handles the space-dependant elevation effect by focusing each channel separately and performing the combination after. In this manner, each target is confined to a limited number of pixels, and topography effects can be adequately compensated locally. Moreover, separating the imaging and

the ambiguity suppression enables a simple processing scheme that utilizes standard focusing tools.

Validation and testing were performed on simulated data, showing good ambiguity suppression for a realistic distributed scene. The positive results encourage the feasibility of the AT train constellation concept, relaxing the requirements on the orbital tube.

References

[1] G. Krieger, N. Gebert, and A. Moreira, "Unambiguous SAR signal reconstruction from nonuniform displaced phase center sampling," *IEEE Geoscience and Remote Sensing Letters*, vol. 1, no. 4, pp. 260–264, Oct. 2004.

[2] M. Grasso, A. Renga, G. Fasano, M. D. Graziano, M. Grassi, and A. Moccia, "Design of an end-to-end demonstration mission of a Formation-Flying Synthetic Aperture Radar (FF-SAR) based on microsatellites," *Advances in Space Research*, vol. 67, no. 11, pp. 3909–3923, Jun. 2021.

[3] J.-P. Aguttes, "Formations oriented along the path of SAR satellites," EP Patent EP1 369 704A1, Dec., 2003.

[4] P. Cheng, J. Wan, Q. Xin, Z. Wang, M. He, and Y. Nian, "An Improved Azimuth Reconstruction Method for Multichannel SAR Using Vandermonde Matrix," *IEEE Geoscience and Remote Sensing Letters*, vol. 14, no. 1, pp. 67–71, Jan. 2017.

[5] D. Giudici, P. Guccione, M. Manzoni, A. M. Guarnieri, and F. Rocca, "Compact and Free-Floating Satellite MIMO SAR Formations," *IEEE Transactions on Geoscience and Remote Sensing*, vol. 60, pp. 1–12, 2022.

[6] T. Kraus, G. Krieger, M. Bachmann, and A. Moreira, "Addressing the Terrain Topography in Distributed SAR Imaging," in *2019 International Radar Conference (RADAR)*, Sep. 2019, pp. 1–5, iSSN: 2640-7736.

[7] O. Dogan, F. Uysal, and P. L. Dekker, "Unambiguous Recovery of Multistatic SAR Data for Nonzero Cross Track Baseline Case," *IEEE Geoscience and Remote Sensing Letters*, vol. 19, pp. 1–5, 2022.

[8] H. Lin, Y. Deng, H. Zhang, D. Liang, and X. Jia, "An Imaging Method for Spaceborne Cooperative Multistatic SAR Formations With Nonzero Cross-Track Baselines," *IEEE Journal of Selected Topics in Applied Earth Observations and Remote Sensing*, vol. 15, pp. 8541–8551, 2022.

[9] N. Petrushevsky, A. Monti Guarnieri, M. Manzoni, C. Prati, and S. Tebaldini, "An Operational Processing Framework for Spaceborne SAR Formations," *Remote Sensing*, vol. 15, no. 6, p. 1644, Jan. 2023, number: 6 Publisher: Multidisciplinary Digital Publishing Institute.

[10] D. Cerutti-Maori, I. Sikaneta, J. Klare, and C. H. Gierull, "MIMO SAR Processing for Multichannel High-Resolution Wide-Swath Radars," *IEEE Transactions on Geoscience and Remote Sensing*, vol. 52, no. 8, pp. 5034–5055, Aug. 2014.

[11] J. T. Johnson, C. J. Baker, G. E. Smith, K. L. Bell, and M. Rangaswamy, "The monostatic-bistatic equivalence theorem and bistatic radar clutter," in *2014 11th European Radar Conference*, Oct. 2014, pp. 105–108.

[12] A. Moreira, P. Prats-Iraola, M. Younis, G. Krieger, I. Hajnsek, and K. P. Papathanassiou, "A tutorial on synthetic aperture radar," *IEEE Geoscience and Remote Sensing Magazine*, vol. 1, no. 1, pp. 6–43, Mar. 2013.

[13] A. Moreira, "Suppressing the azimuth ambiguities in synthetic aperture radar images," *IEEE Transactions on Geoscience and Remote Sensing*, vol. 31, no. 4, pp. 885–895, Jul. 1993.

[14] N. Petrushevsky, A. Monti-Guarnieri, and S. Tebaldini, "Exploiting Ambiguities for Along-Track Baseline Calibration of SIMO SAR Formations," in *IGARSS 2023 - 2023 IEEE International Geoscience and Remote Sensing Symposium*, Jul. 2023, pp. 7781–7784, iSSN: 2153-7003.

[15] F. Gatelli, A. Monti Guarnieri, F. Parizzi, P. Pasquali, C. Prati, and F. Rocca, "The wavenumber shift in SAR interferometry," *IEEE Transactions on Geoscience and Remote Sensing*, vol. 32, no. 4, pp. 855–865, Jul. 1994.